Emergent Materials
https://doi.org/10.1007/s42247-024-00759-1

ORIGINAL ARTICLE

Synthesis of mesoporous structured $ZnMn_2O_4$ nanoparticles as electrode for supercapacitor application

P. Deva[1] · S. Ravi[1] · C. Manoharan[1]

Received: 20 March 2024 / Accepted: 29 May 2024

Abstract
Spinel $ZnMn_2O_4$ has been gaining more attention in the realm of supercapacitor applications due to its accessibility, affordability, sustainability, high specific capacitance, and excellent rate capability. In this study, spinel $ZnMn_2O_4$ was synthesized using a rapid, eco-friendly citric acid-mediated sol–gel auto-combustion approach. A thorough study was conducted to correlate the phase structure, surface morphology, functional groups, oxidation states, specific surface area, and redox reaction of the electroactive species with their potential impact on the electrochemical behaviour of electrode material. The prepared spinel $ZnMn_2O_4$ electrode material showed an impressive specific capacitance value of 417.5 F g^{-1} under low electrolyte concentrations and a current density of 1 A g^{-1}. In an aqueous electrolyte, the reaction kinetics of the supercapacitor become very fast and this is responsible for its high capacitance. An excellent coulombic efficiency of 87% was obtained for this electrode material even after 5000 cycles. The exceptional electrochemical performance is mainly attributed to the nanoparticles, which have a large reaction surface area, fast transfer of ions and electrons, high ionic conductivity, and excellent structural durability. These significant results emphasize the $ZnMn_2O_4$, potential as a supercapacitor material.

Keywords Spinel $ZnMn_2O_4$ · Autocombustion · Specific surface area · Aqueous electrolyte · Energy storage device

1 Introduction

The demand for sustainable and clean energy sources has intensified because of increased pollution and the depletion of fossil fuels. Batteries and supercapacitors have generated attention as viable systems for storing energy from renewable sources, thanks to their effective performance. Nonetheless, these systems encounter challenges, such as the demand for smaller, lighter and more flexible devices with high energy and power densities. The long cycle and affordability of supercapacitors have become a focal point for researchers due to their advantageous characteristics, promoting the exploration of various approaches to enhance their energy storage [1, 2].

Supercapacitors (SCs) have attracted considerable attention of researchers, because they can capitalize on their beneficial features. Many approaches for the provision of electrode materials have been explored to enhance their energy density. The three main types of supercapacitors are: i) electrochemical double-layer capacitors (EDLC non-Faradaic), ii) pseudocapacitors (Faradaic), and iii) hybrid capacitors (a combination of the two), [3, 4]. Electrochemical capacitors typically use carbon [5], transition metal oxides [6, 7], and electrically conductive polymer [8] as electrode materials. Both advantages and disadvantages are included. Although carbon is known to have low specific capacitance, it also exhibits excellent conductivity and cycle stability. On the other hand, conducting polymers exhibited lower specific capacitance when compared to metal oxides. Transition metal oxides are known for their large capacities and rapid charging capabilities. Consequently, transition metal oxides are of utmost importance in global research.

Manganese-based transition metal oxides TMOs, like MnO_2 [9], Mn_2O_3 [10], and Mn_3O_4 [11], present intriguing prospects due to cost-effectiveness, environmental friendliness, and a wide range of oxidation states, manganese from +2 to +7,contributing to a high specific capacitance. Nevertheless, their limited conductivity and expansion in volume during charging and discharging restrict their practical use. Currently, researchers are working on spinel structures of mixed transition metal oxides (MTMOs), due to their high electrochemical

✉ S. Ravi
ambedravi1975@gmail.com

[1] Department of Physics, Annamalai University, Annamalai Nagar, Chidhambaram 608 002, Tamil Nadu, India

Published online: 10 June 2024

performance and overall chemical composition of AB_2O_4 [12]. Hence, this type of material is of great interest because of its various features, such as photocatalytic [13], sensor [14], electrochemical performance [15, 16], magnetic properties [17], and application in lithium-ion batteries [18, 19]. Spinel- structured ternary manganese oxides are $CoMn_2O_4$ [12], $NiMn_2O_4$ [20], $ZnMn_2O_4$ [15], and $CuMn_2O_4$ [21]. $ZnMn_2O_4$, is known for its energy storage capabilities, features Zn^{2+} ions in tetrahedral sites and trivalent Mn^{3+} ions octahedral sites. As an energy storage material, $ZnMn_2O_4$ offers advantages like low working potential, being non-toxic, having a high energy density, and plentiful raw materials when compared with to other spinel electrode materials. [22].

Numerous approaches, such as solvothermal [23], co precipitation [24], hydrothermal [25],electrospinning [26], sol–gel[27], and combustion [28] processes, have been used in the synthesis of $ZnMn_2O_4$ materials with varying microstructures. Among these synthesis approaches, the one-pot solution combustion approach is the most desirable, because it has an affordable high yield with cost-effective precursors, can be used for large-scale production, requires little else, and allows for quick reactions to complete crystallization [29]. $ZnMn_2O_4$ has been identified by numerous researchers as an ideal material for electrochemical applications. Recent studies, Sathiyamoorthi et al., (2020) reported a carbon- $ZnMn_2O_4$ material Cs of 118 F g^{-1} at 0.1 A g^{-1} [30].Abdollahiafar et al. (2018) reported a carbon-coated $ZnMn_2O_4$ nano crystallite with a Cs of 150 F g^{-1} [28]. Guo et al. (2015) reported spinel porous $ZnMn_2O_4$ which exhibited a Cs value of 158 F g^{-1} for scan rate of 2 mVs^{-1} [31]. Bhagwan et al.(2018) reported a Cs value of 240 F g^{-1} for 1 a g^{-1} [32]. Puratchi Mani et al.(2021) reported that cubic-like $ZnMn_2O_4$ achieves a Cs value of 776 F g^{-1} for the scan rate of 5 mVs^{-1} [22]. Recently, Yang et al. used a surfactant-assisted way for the synthesis $ZnMn_2O_4$/Mn_2O_3 composite, following calcination at 600 °C which demonstrated its exceptional performance in zinc-ion batteries applications [33].

In this study, spinel $ZnMn_2O_4$ was synthesized using a rapid, eco-friendly citric acid-mediated sol–gel auto-combustion approach at varying calcination temperatures. The calcined sample $ZnMn_2O_4$ electrodes exhibited high specific capacitance, effective high-current capacitive behaviour, and excellent cycle performance. The enhanced electrochemical behaviour of the prepared materials suggested that the obtained nanomaterials are beneficial for supercapacitor applications.

2 Materials and methods

2.1 Materials

Zinc nitrate hexahydrate (98%), Manganese nitrate hexahydrate (99.9%), citric acid (99.5%) and ammonia (99.9%) were procured from Sigma- Aldrich Chemical Co. in their original analytical reagent grade state, without undergoing any additional purification process.

2.2 Preparation of $ZnMn_2O_4$ (ZMO) Nanoparticles using Auto-Combustion Method

The precursor materials, manganese nitrate and zinc nitrate with molar ratio 2:1 were dissolved in distilled water. Then, citric acid ($C_6H_8O_7$) was added with the precursor solution which was under continuous stirring under room temperature. The pH of the solution was maintained at 7.0 by adding ammonia (NH_3) drop wise, which led to the formation of a consistent brown solution (sol). The presence of ammonia in the sol–gel process can help control the gel formation and stabilize the precursor solution, resulting in uniform and well-defined structures.. The sol solution was stirred at 80°Cfor 3 h, which induce the dehydration and lead to form viscous gel. Following this, the viscous gel was placed on hot plate at 120 °C until the formation of powder by burning.The obtained powder after burning was annealed at different temperatures (600, 700, and 800 °C) for about 3 h. These synthesis processes are represented by Eq. (1).

$$Zn(NO_3)_2.6H_2O + 2Mn(NO_3)_2.6H_2O + 3C_6H_8O_7 \rightarrow ZnMn_2O_4 + 18CO + 3HNO_3 + 3NH_3 + 24H_2O + O_2 \quad (1)$$

2.3 Material characterization

The ZMO samples underwent TG/DTA analysis on (NETZSHSTA 449 F3JUPITER) instrument with heating rate of 10 °C min^{-1} from ambient temperatures to 1000°C. X-ray diffraction technique was utilized to examine crystal structure, material formation, and phase structure by recording spectrum ranging from 10–80 °.The diffraction patterns were generated by using an HTK1200N-Bruker D8). FESEM was used to analyse the morphology of the synthesised particles using (CARL ZEISS-SIGMA300). The FTIR spectra were recorded for the synthesized ZMO sample using Bruker optic GMBH instrument. XPS was employed to analyze the oxidation states of (Zn), (Mn), and (O) elements on the sample surface. The BET technique was utilized to explore the specific surface area and available pore size.

2.4 Electrode preparation for supercapacitor

The nickel-foam electrode was cleaned using double distilled water followed by, acetone rinsing and air-drying. An active material mixture, including 80% $ZnMn_2O_4$, 10% of carbon black, 10% of polyvinylidene difluoride (PVDF), and a few drops of N-methyl-2-pyrrolidone

(NMP) was then applied to the Ni-foam, followed by an 80 °C in a hot air oven for 24 h to eliminate the NMP. Electrochemical investigations were then carried out using a three-electrode system. ZMO coated Ni-foam acted as the working electrode, whereas Ag–AgCl, and Pt wire acted as the reference and counter electrodes, respectively. The tests included cyclic voltammetry (CV), galvanostatic charge–discharge (GCD), cycle stability, and electrochemical impedance spectroscopy (EIS) in a 1 M KOH aqueous solution. Various scan rates ranged from 5—100 mV s^{-1} and current densities from 1—5 A g^{-1} were employed for CV and charge –discharge test, within specific potential windows. The EIS spanned a frequency range of 0.01 Hz–100 K Hz. The Cs was evaluated by Eq. (2) and (3) [34].

$$C_s = \frac{\int I(V)dV}{mv\Delta V} \tag{2}$$

The specific capacitance Cs was determined for CV, where I (V) represent the curve's area, m-mass of the electrode (g), v- scan rate (mV s^{-1}) and ΔV—potential window operation.

$$C_s = \frac{Idt}{m\Delta V} \tag{3}$$

The Cs specific capacitance calculated GCD, I dt is the charge and discharge.

The ZMO electrode material electrochemical characteristics, including columbic efficiency (η, %), energy density (E, W hkg^{-1}), and power density (P, W kg^{-1}) were computed using Eq. (4), (5), and (6) respectively [35, 36].

$$\eta = \frac{t_d}{t_c} \times 100 \tag{4}$$

$$E = \frac{1}{2 \times 3.6} C_s(\Delta V)^2 \tag{5}$$

$$P = \frac{E \times 3600}{\Delta t} \tag{6}$$

Cs represents the specific capacitance determined from Eq. (3), the potential window V, and charge–discharge times t_c and t_d.

3 Result and Discussion

3.1 Thermal stability analysis

Thermogravimetric differential thermal analysis (TG–DTA) was carried out to explore the phase transitions, decomposition process, crystallization behaviour, and thermal stability of the synthesised sample. Figure 1 indicates that the as-prepared metal precursors degraded in three steps. The initial step occurs below 154 °C, where a steady weight loss of 8.05% occurs that may be attributed to the evaporation of the absorbed moisture and residual substances. Subsequently, a weight loss of approximately 15.62% upto 423 °C may be ascribed to decomposition and the removal of residual carbon [28]. The observed third weight loss of 11.12% upto 559 °C was due to the degradation of small amounts of metal nitrates and formation of metal oxide nanocrystals. Therefore, to remove residual nitrates and to synthesize nanomaterials with excellent crystallinity, the precursor was calcined at 600, 700, and 800 °C for 3 h in an air atmosphere to obtain a brown product.

3.2 Structural analysis

The analysis of the $ZnMn_2O_4$ material's phase purity, crystal structure, and crystallinity was conducted through powder XRD analysis. The XRD patterns of the $ZnMn_2O_4$ nanoparticles (NPs) recorded after calcination at temperatures 600, 700, and 800 °C are shown in Fig. 2. The samples calcined at temperatures 600, 700, and 800 °C are designated as ZMO-600, ZMO-700, and ZMO-800, respectively. The diffraction peaks matched with the $ZnMn_2O_4$ tetragonal phase of standard JCPDS No. 77–0470 and the phase group $I4_1/amd$ [22]. The absence of additional impurities suggests that the obtained powder is indeed of high purity. The reflection peaks were indexed to the various (hkl) planes (101) (112) (200) (103) (211) (004) (220) (204) (105) (312) (303) (321) (224) (400) and (413) seen at 2 θ values 18.20, 29.30, 31.26, 33.06, 36.41, 38.87, 44.80, 50.23, 51.95, 54.41, 56.71,

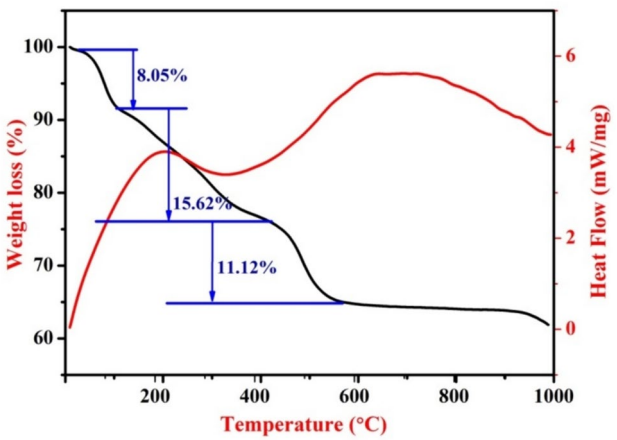

Fig. 1 TG–DTA curve of the $ZnMn_2O_4$ as-prepared precursor

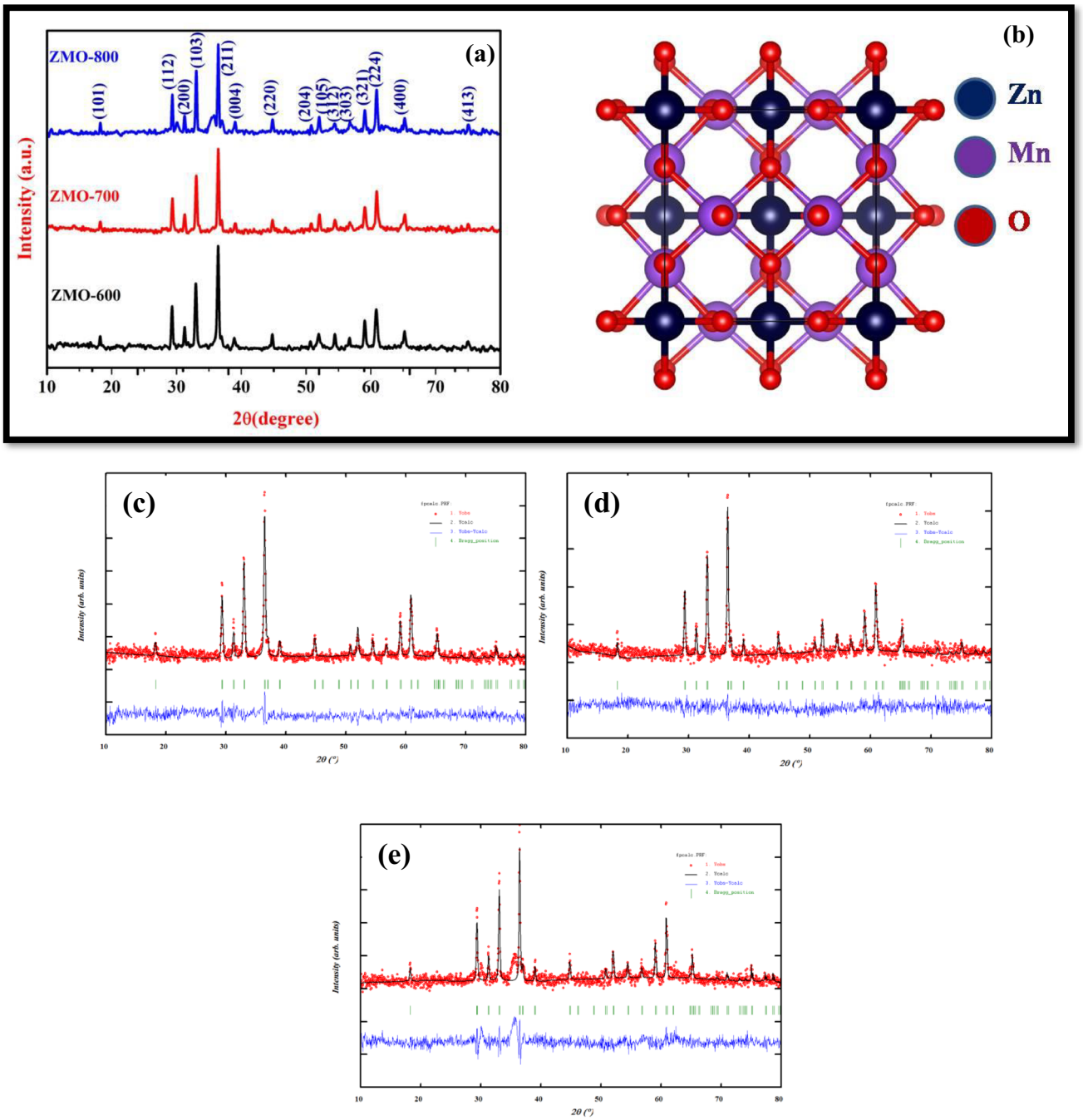

Fig. 2 (**a**) XRD spectra of $ZnMn_2O_4$ (**b**) crystal structure of $ZnMn_2O_4$ spinel (**c**-**e**) Rietveld fitting for (**c**) ZMO-600, (**d**) ZMO-700, and (**e**) ZMO-800 samples

59.01, 60.77, 65.22, and 75.05, respectively. The increased Full Width at Half Maximum (FWHM) of all peaks suggested the reduction in particle size [37]. The average crystallite size of the $ZnMn_2O_4$ powder was approximately 32, 35, and 43 nm, as determined by Sherrers' Eq. (7).

$$D = \frac{0.94 \times \lambda}{\beta Cos\theta} \tag{7}$$

where (λ): X-ray wavelength, (β)*:* Full-width half- maximum (FWHM), and (θ): diffraction angle.

The lattice parameters, volume (V), dislocation density (δ), and the microstrain (ε) are computed:

$$a = d_{hkl}\sqrt{h^2 + k^2 + l^2} \tag{8}$$

$$V = a^3 \tag{9}$$

$$\delta = \frac{1}{D^2} \tag{10}$$

$$\varepsilon = \frac{\beta Cos\theta}{4} \tag{11}$$

The Miller indices, volume (V), and (D) crystal size are characterized by interplanar distance (d_{hkl}) and, hkl planes.

The Rietveld refinement conducted on the ZMO-600, ZMO-700, and ZMO-800 samples is depicted in Figs.2 (c-d). This refinement was concentrated on the phase purity, structure and identification of all peaks. The XRD data obtained from calculations closely matched the experimental data, with minimal differences observed. In the graph, the red represents the observed data, while black solid line represents the calculated XRD peak intensities. The vertical green lines indicate the Bragg positions, and the blue color highlights the disparities between experimental and observed intensities. Throughout the refinement process, no impurity peaks were detected except for ZnMn2O4. The goodness of fit (χ^2) ranged from 0.7 to 1.3.

Table 1 presents lattice and structural parameters of the samples. The crystallite size increased with the increasing calcination temperature. The crystallite size of the samples calcined at 600 °C, seems to be small and no impurities are detected. As the crystallite and grain size plays major role in specific surface area, the sample calcined at 600 °C is selected as the crystallite size seems small at this temperature. The smaller crystal size contributes to improved dielectric properties, primarily due to factors such as increased grain boundaries, which can induce a polarization effect. Further surface investigations using additional surface characterizations were conducted on ZMO-600. In the crystallographic information, $ZnMn_2O_4$ has a standard spinel structure where Zn^{2+} ions are stacked in tetrahedral positions, while Mn^{3+} ions occupy octahedral sites, resulting in ZnO_4 and MnO_6 groups, respectively. This crystal arrangement is depicted in detail in Fig. 2b. Moreover, $ZnMn_2O_4$ being isostructural with Mn_3O_4, enables efficient adsorption of Zn^{2+} ions into the tetrahedral site of the Mn_3O_4 lattice without separation, generating normal spinel $ZnMn_2O_4$ with the substitution of Mn^{2+} and Zn^{2+} [38].

3.3 Morphology Analysis

The morphology (size and shape) of the synthesized materials plays a crucial role in specific application like photocatalytic and electrochemical performance. The FESEM images recorded for the calcined samples are shown in Fig. 3. The images a, c, and e are with low magnification whereas b, d, and f are with higher magnification of the samples ZMO-600, ZMO-700, and ZMO-800 respectively. The agglomeration observed in the lower and higher magnifications of the images was due to existence of the attractive force (magnetic force).Generally, the material $ZnMn_2O_4$ with spinel like structure possess antiferromagnetic behaviour (Ref). When nanoparticles are magnetic they can attract each other due to magnetic dipole–dipole interaction, which leads to agglomerations. Also the other important factor such as Van der Waals forces, electrostatic interactions and solvents effects can also play significant roles in agglomeration [39]. Detailed examination of the low and high magnification images revealed a compact agglomeration with multiple tiny holes that provide smooth ion diffusion in the $ZnMn_2O_4$ material. The presence of numerous voids, on the surface facilitated the passage of ions into the interior and the intercalation of KOH ions into the structure. Nanoparticles exhibiting this agglomeration shape offer increased active surface areas, open spaces, and enhanced electrical contact, potentially leading to superior electrochemical performance.

The ED investigations were carried out to analyze the elemental composition within $ZnMn_2O_4$, Fig. 3. This study confirmed the uniform- distribution of elements of Zn, Mn, and O with an Mn/Zn atomic ratio equal to the

Table 1 XRD parameters of the prepared zinc manganese oxide

S No	Sample Name	Crystallite Size (nm)	Micro Strain (ε)$\times 10^{-3}$	Dislocation Density (δ)$\times 10^{-15}$	Lattice Parameter (Å) a = b ≠ c a = 5.720, c = 9.240	Volume Å^3 V = 302.32
1	ZMO-600	32	1.09	1.48	a = 5.716 c = 9.225	301.509
2	ZMO-700	35	0.99	1.48	a = 5.718 c = 9.250	302.510
3	ZMO-800	43	0.84	1.07	a = 5.719 c = 9.228	301.842

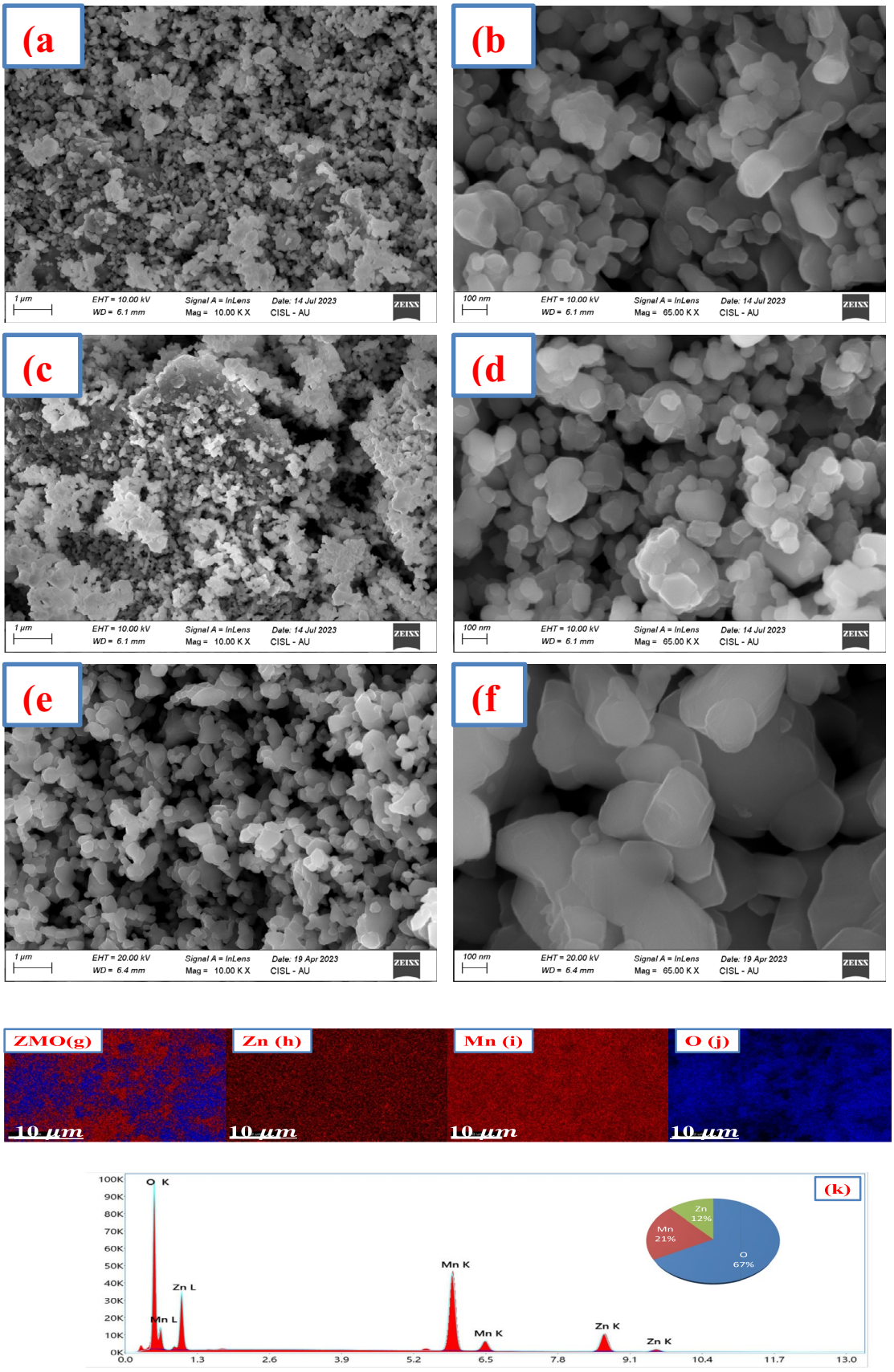

Fig. 3 FESEM images ZMO-600 (**a** and **b**), ZMO-700 (**c** and **d**), ZMO-800 (**e** and **f**), elemental mapping (**g**-**j**) and (**k**) EDS spectrum

expected value of 1.86 Fig. 3 (g-k). In addition, absence of other elements in the EDX spectrum confirms the purity of the prepared sample $ZnMn_2O_4$.

3.4 FTIR analysis

The Fourier- transform infrared (FT-IR) analysis of the nanomaterials revealed the presence of functional groups included surface-absorbed molecules of $ZnMn_2O_4$ Fig. 4. The spectrum was recorded within the wave number 4000—400 cm^{-1} range. The broad absorption that at from 3451 cm^{-1} to 2918 cm^{-1} could include stretching vibrations of hydroxyl groups (-OH) and symmetric stretching of CH_2 groups [32, 40]. The near-weak band at 1633 cm^{-1} was ascribed to C-N or C = O functional groups [32]. Moreover, three distinct absorption bands ranging from 400 to 700 cm^{-1}, with peaks 630 cm^{-1}, 524 cm^{-1} and 417 cm^{-1} indicated the presence of M–O-M and M–O (where M = Zn, Mn) vibrations [22]. Finally, the experimental absorption bands detected at lower frequencies suggested the arrangement of $ZnMn_2O_4$ spinel structure.

3.5 XPS analysis

The optimized sample's (ZMO-600) chemical composition and chemical states analyzed utilizing X-ray photoelectron spectroscopy (XPS) are shown in Fig. 5. The survey spectrum of the composite indicates the existence of Zn, Mn, O, and C without any detectable differences from other elements. The high resolution spectra of Zinc, Manganese, and Oxygen recorded for detailed analysis are shown in Fig. 5 (a).The analysis of Zn2p spectra in Fig. 5(b) displays two peaks at 1021.6 and 1044.5 eV attributed to $Zn2p_{3/2}$ and $Zn2p_{1/2}$, respectively, with a binding energy difference value of 23.1 eV consistent with the Zn^{2+} oxidation state [41]. Similarly, the Mn2p spectrum splits into $Mn2p_{3/2}$ and $Mn2p_{1/2}$ due to a local magnetic field, with binding energy values of 642.1 and 653.9 eV respectively, indicating the binding energy difference between the two levels approximately 11.8 eV, indicating the oxidation state of Mn as 2^+ [42]. The fitted peaks at 641.1 and 652.9 eV correspond to the Mn^{2+} oxidation state, while those at 643.3 and 654.8 eV represent the Mn^{3+} oxidation state. The O 1 s peaks reveal three fitted peaks at 529.8, 530.9, and 532.4 eV linked to the metal–oxygen (M–O) band, hydroxyl (OH) bond, and lattice oxygen, respectively [42]. Therefore, the synergism of Zn and Mn ion's distinct valences may significantly improve the electrochemical performance of spinel $ZnMn_2O_4$ nanomaterials.

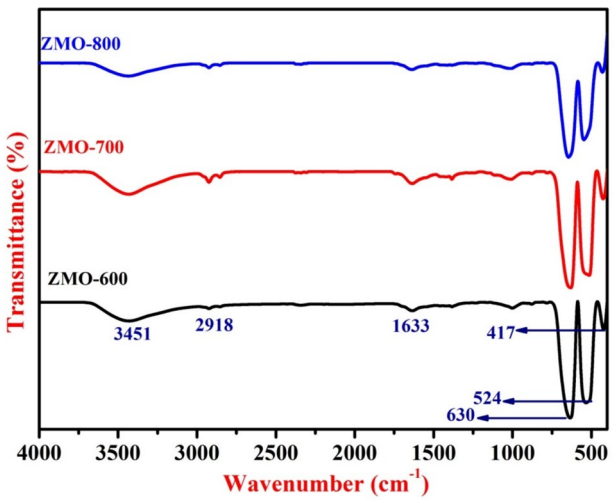

Fig. 4 FT-IR spectrum of $ZnMn_2O_4$ nanoparticles

3.6 Textural Analysis

The textural properties of the optimized ZMO-600 materials were evaluated through nitrogen adsorption–desorption isotherm measurements were illustrated in Figs. 6 (a and b). The results from the N_2- isotherm analysis classified the materials as having a Type IV isotherm as per the IUPAC standards. Moreover, the ZMO-600 materials demonstrated a specific surface area of 284.14 $m^2\ g^{-1}$ [43]. The pore size distribution analysis of nanoparticles indicated the mesoporous structure with a diameter of 2.35 nm with non-uniform in size. Overall, the N_2 adsorption–desorption isotherm investigations found that the materials possess a suitable mesoporous texture with a significantly high surface area, aiding in transport and diffusion of electrolyte ions into electrode throughout charge–discharge processes. The anticipated enhancement is expected to result in improved electrochemical performance, characterized by elevated high Cs and enhanced cyclic stability.

3.7 Dielectric properties

3.7.1 Dielectric constant and loss properties

The dielectric properties of the optimized sample ZMO-600, including the dielectric constant (ε) and dielectric loss (tan δ) are depicted in Fig. 7 (a and b) at room temperature across frequencies. The characteristics of dielectric materials depend on many factors, such as the technique used to prepare the sample, cation substitutions, and grain size. Polycrystalline substances serve as heterogeneous dielectrics, featuring individual high-conductivity grains isolated by low-conductivity grain boundaries [32]. The capacitance (Cp), impedance (Z), and loss tangent (tan δ) were

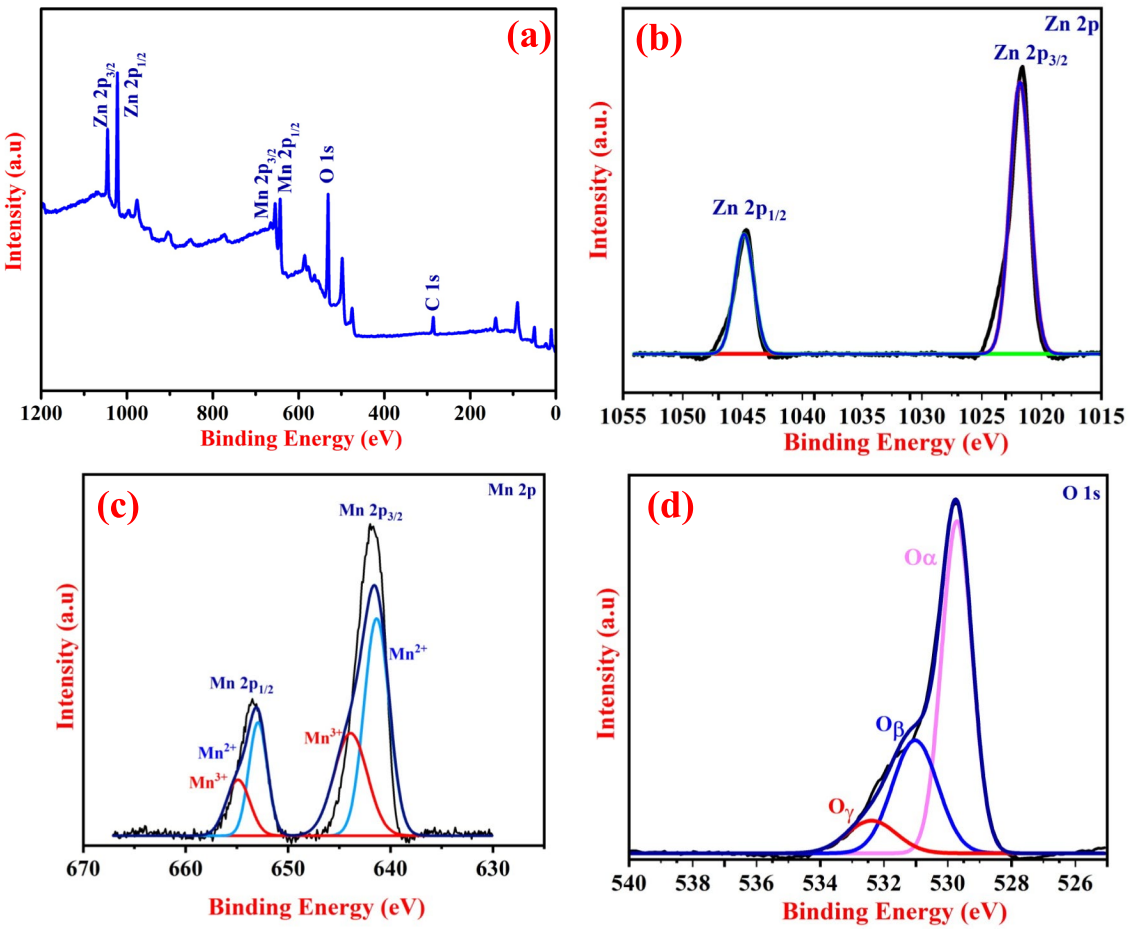

Fig. 5 (**a**) XPS survey spectrum (**b**) Zn 2p (**c**) Mn 2p and O 1 s

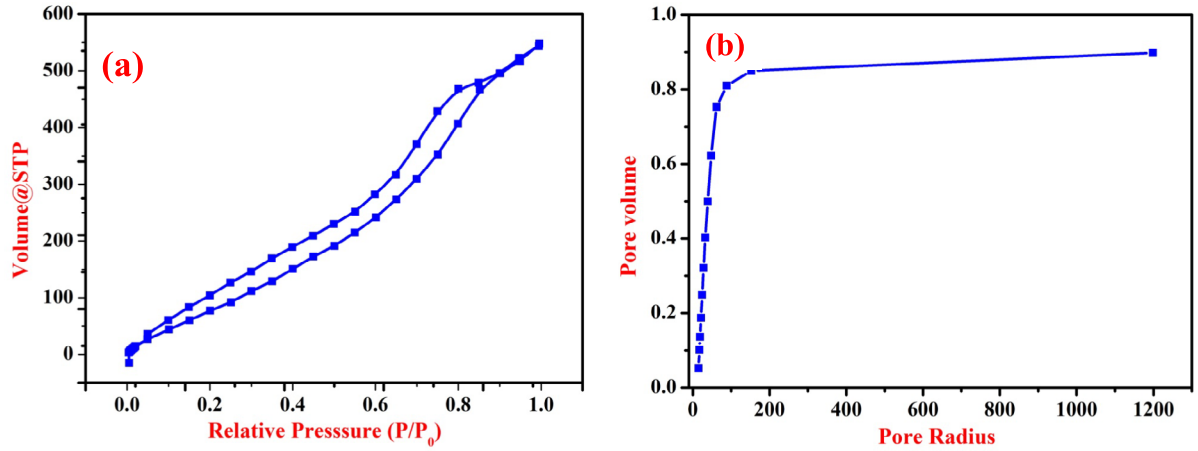

Fig. 6 (**a**) Nitrogen adsorption–desorption isotherms (**b**) pore size distribution curve

calculated to assess the dielectric and AC characteristics [43]. $\varepsilon\prime = \frac{C_P \times t}{\epsilon_0 \times A}$, where t, represents the thickness of the pellet, A the area of the pellet,$\varepsilon'' = \varepsilon\prime \times tan\delta$, and $\sigma_{ac.tot}(\omega) = \frac{t}{ZA}$. The value of dielectric constant diminishes gradually with increasing frequency, and becomes stable at higher frequencies, based on Wanger form [44]. Several factors,

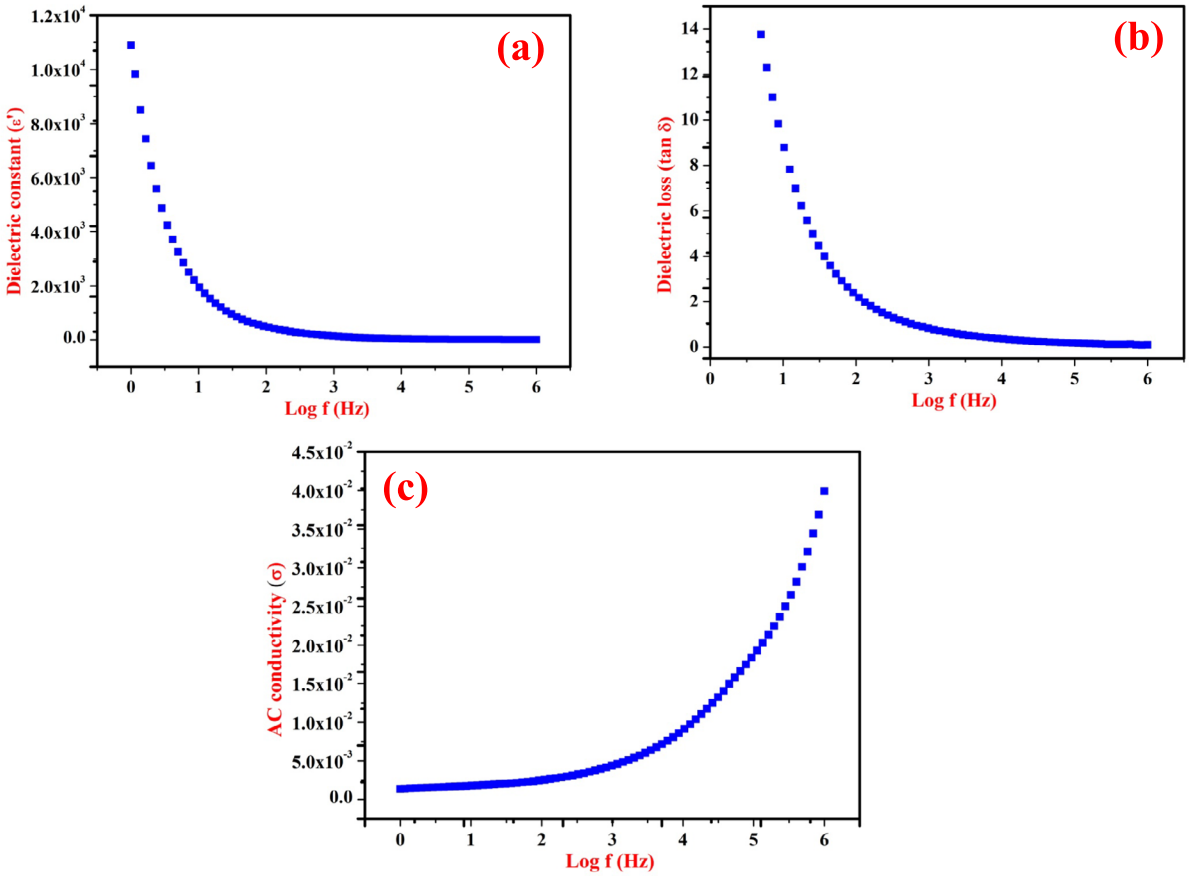

Fig. 7 (**a**) Dielectric constant (**b**) Dielectric loss and (**c**) AC conductivity of $ZnMn_2O_4$

such as time relaxation and the role of grain boundaries and grains, have been suggested to explain the high dielectric constant at lower frequencies in nanomaterials. In lower frequency areas, dipoles can align with the electric field due to sufficient time, with grain boundaries playing a significant role in the dielectric constant enhancement. This phenomenon can be explained based on **Koop's model**. Grain boundaries play a greater role at low frequencies, where the higher dielectric constant contribution is mainly due to grain boundaries. At low frequencies, space charge follow the applied electric field, while there is no enough time to build up at higher frequencies [45]. Additionally, it has been observed in alloy nanomaterials that the role of grain boundaries in increasing the enhanced dielectric constant at low frequencies surpasses that of the grains themselves [46]. Space charge polarization contributes to high dielectric constant values by actively participating in polarization at lower frequencies. On the contrary, in high-frequency regions, dipoles struggle to align with the field, resulting in decreased dielectric constant values [47]. The dielectric loss decreased notably between 0–3 MHz frequencies and remained consistent from 4–6 MHz frequencies Fig. 7 (b) shows the dielectric loss trend against frequency regions.

3.7.2 AC conductivity

Figure 7 (c) shows the relationship between AC conductivity and frequency at room temperature for spinel ZMO-600. A noticeable enhancement in AC conductivity is evident at higher frequencies. The entire frequency range exhibits relaxation, characterized by gradual increase in conductivity. The behavior of the dielectric constant can be explained by the free dipole oscillating field which shows a correlation between relaxation time and frequency. At very low frequencies, the dipoles lag behind the field, leading to a conductivity improvement. Conversely, at very high frequencies, the dipole exhibits frequency independence, resulting in a rapid conductivity surge [48]. As the frequency increases, the hopping frequency among charge carriers also escalate, further boosting conductivity.

3.8 Electrochemical measurement of $ZnMn_2O_4$ electrode material

3.8.1 CV analysis of ZMO-600

The electrochemical property of ZMO-600 electrode system was examined using three-electrode configurations with

1 M KOH electrolyte solution. Aqueous electrolytes used in the present study have unquestionable advantages of low price, low toxicity, and safety and more importantly they allow high power capabilities [49]. Cyclic voltammetry evaluation of the $ZnMn_2O_4$ electrode materials was conducted and shown in Fig. 8. (a) These evaluations displayed distinct redox peaks for the $ZnMn_2O_4$ materials. The ZMO-600 material's cyclic voltammogram exhibited two peaks at 0.38 and 0.26 V when scanned at a rate of 5 mVs^{-1}, indicating the presence of Faradaic oxidation and reduction processes, respectively on its surface material. These findings suggest pseudocapacitor behavior of the material.

The electrochemical reaction occurs through the Faradaic de/adsorption and de/intercalation processes. [50–52]. The electrochemical reaction occurring within the electrode material could be formulated as follows:

$$ZnMN_2OH + OH^- + H_2O \leftrightarrow ZnOOH + 2MnOOH + e^- \quad (12)$$

$$MnOOH + OH^- \leftrightarrow MnO_2 + H_2O + e^- \quad (13)$$

$$\left(ZnMn_2O_4\right)_{surface} + K^+ + e^- \rightarrow \left[KZnMn_2O_4\right]_{surface} \quad (14)$$

$$ZnMn_2O_4 + K^+ + e^- \rightarrow \left[ZnMn_2O_4\right]K \quad (15)$$

Based on the CV curves, it was identified that the developed ZMO-600 material displayed a very small potential shift, with increasing scan rate. The observed shift in the redox peak at higher scan rates is due to diffusion resistance and polarization effects. Furthermore, the significant current seen at higher scan rates is attributed to the efficient electronic and ionic transport within the electrode material [15]. The (Cs) of the electrode material was calculated by employing Eq. (2).

3.8.2 GCD analysis and cyclic behaviour of ZMO-600 as electrode material

To confirm the specific capacitance and potential application of the optimized sample ZMO-600, GCD measurements were carried out with a 1 M KOH solution within the potential window range of 0 to 0.40 V at various current densities ranging from 1 to 5 A g^{-1}. Figure 9 (a) represents the charge and discharge curves at different current densities. Notably, the potential-time curves exhibited symmetrical patterns across different current densities, indicating high coulombic efficiency. Moreover, the non-linear charge/discharge curves reaffirmed the pseudocapacitance behaviour of the sample. The value of specific capacitance was determined using Eq. (3) from the GCD curves. The specific capacitance as a function of current densities is illustrated in Fig. 9 (b), The specific capacitance of ZMO-600 is 417.52, 375.43, 330.04, 290.13, and 262.65 F g^{-1} at various current densities1, 2, 3, 4, and 5 A g^{-1}, respectively. The decrease in specific capacitance with increasing current density can be ascribed to the diffusion process of a OH^- ion during charging and discharging of electrode. As the discharge current density increases, there's a greater demand for sizable OH^- ions to quickly integrate at the boundary between electrode and the electrolyte [51]. The remarkable rate capability displayed by the electrode material renders it, as a promising material for practical applications, indicating a specific capacitance with high currents densities and low electrode polarization.

The durability of the sample's electrochemical stability of the sample is best represented by cycle performance. The

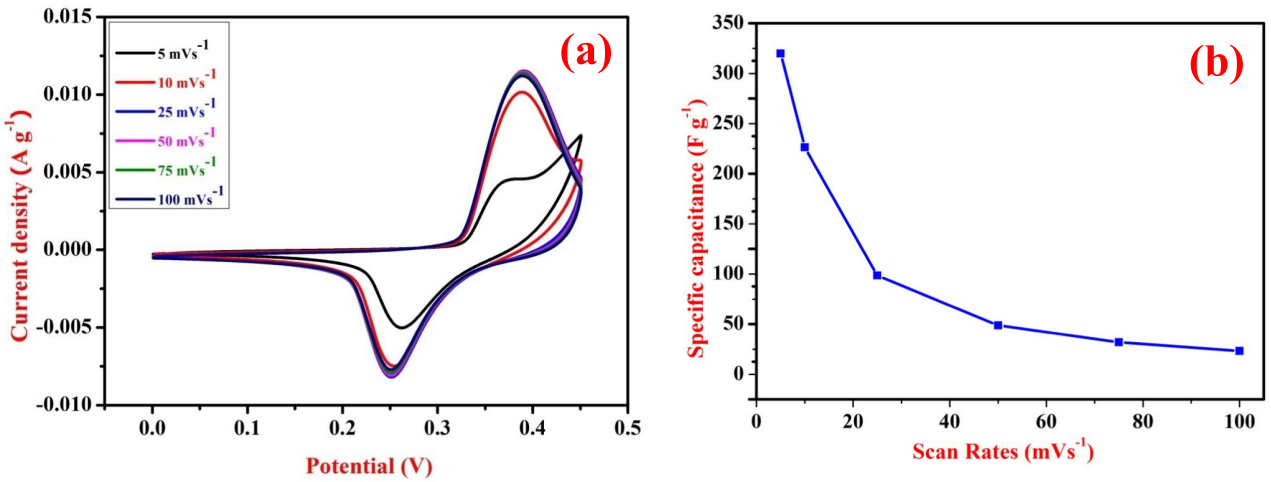

Fig. 8 (**a**) CV curves of ZMO-600 at various scan rates range from 5 mVs^{-1} to 100 mVs^{-1} (**b**) Calculated specific capacitance of ZMO-600 sample function of the scan rates

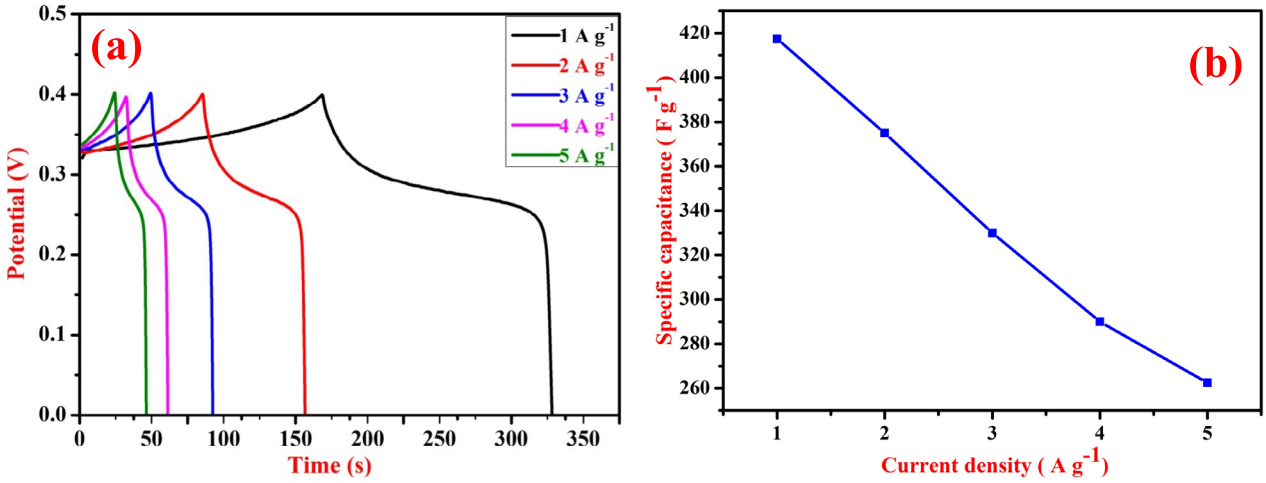

Fig. 9 (**a**) GCD curves of ZMO-600 electrode material at various current densities (**b**) Specific capacitance comparison of current densities

evaluated long-term analysis of the ZMO-600 electrode material with 5000 cycles at 5 A g^{-1} using GCD cycling is shown in Fig. 10 (a). The observed specific capacitance value remained unchanged for the entire cycle. This demonstrates the structural stability and consistency of the ZMO-600 electroactive material. The consistency of specific capacitance value even after 5000 cycles evidenced the stability of the electrode material. The capacity retention and coulombic efficiency of the ZMO-600 electrode material was calculated using Eq. (4 and 4a).The electrode materials have a coulombic efficiency of 87% even after 5000 cycles through charge–discharge curves, indicating their long-term performance due to their improved electrochemical characteristics. The high coulombic efficiency of 87% at 5000 cycles with the capacity retention around 100% suggesting the material good stability with low degradation. The high coulombic efficiency leads capacity retention contributes to a longer cycle life. The excellent performance of supercapacitors can be attributed to their key attribute: energy and power density. The (E) and (P) were computed using the GCD analysis following Eq. (5) and (6), respectively. The Ragone plot of Fig. 10 (b) represents E Vs P. The device exhibited maximum calculated E and P values of 5.83 whkg^{-1} and 1000 wkg^{-1}, for current density of 5 A g^{-1}. Overall, the electrochemical characteristics, surface shape, and specific surface area enhanced the number of active sites due to the deep electrolyte penetration. These observed electrochemical results suggested that the distinctive $ZnMn_2O_4$ electrode material is ideal for supercapacitor applications. In comparison to previously reported values in the literature, the cyclic stability of the synthesized $ZnMn_2O_4$ sample in this study exhibited enhanced specific capacitance and colulombic efficiency with a lower concentration of 1 M KOH electrolyte Table 2 [53].

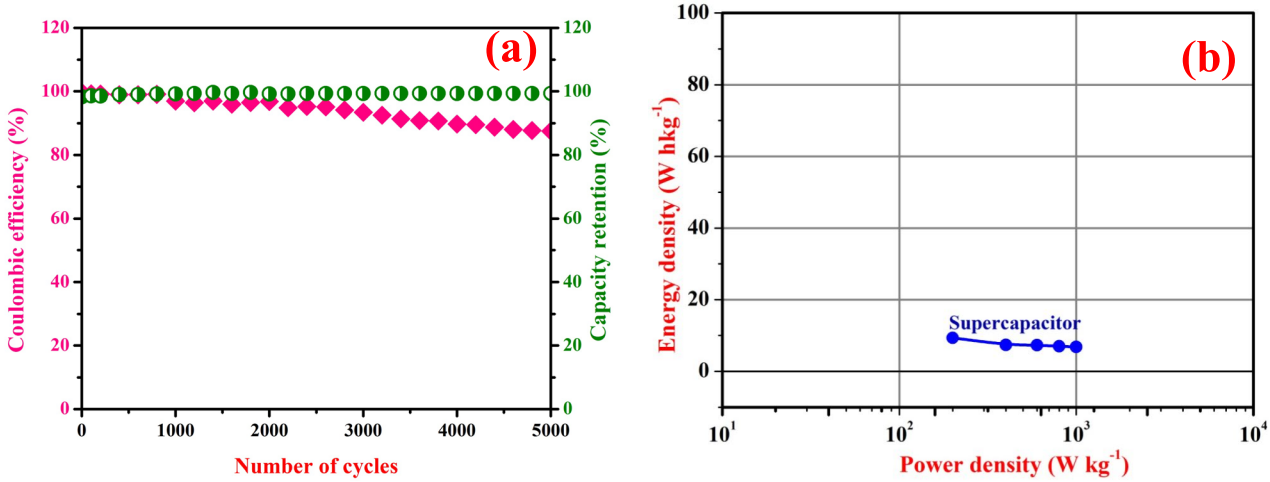

Fig. 10 (**a**) Coulombic efficiency of ZMO-600 (**b**) Ragone plot

3.8.3 Electrochemical impedance spectroscopy (EIS) of ZMO-electrode material

The study explained the process of energy storage through EIS. By utilizing a three-electrode configuration, the electrode material allowed for the continuous monitoring of electrode/electrolyte interactions. The impedance analyses were conducted utilizing a 1 M KOH as the aqueous electrolyte within a frequency range 0.01–100 kHz. The impedance spectroscopy provides information on the internal structure and dynamics of the material. Various factors, such as sample structure, crystal imperfections, and other relevant elements, were found to have a significant impact on the impedance spectroscopy of materials. Figure 11 shows the impedance spectroscopy result for ZMO-600. The impedance plot consists of one semicircle component at high frequencies, succeeded by a linear line at low frequencies. The semicircle represents the pseudo-charge transfer resistance (Rct). The ZMO-600 exhibited a charge-transfer resistance of approximately 1.28 Ω. Conversely, the straight line at lower frequencies indicated the presence of diffusive resistance Warburg impedance caused by the movement of electrolyte ions within host substance [15, 51]. Both cyclic voltammetry and EIS measurements indicated the good pseudocapacitive nature of $ZnMn_2O_4$.These results indicate that the synthesized $ZnMn_2O_4$ nanomaterial is highly appropriate for enhanced conductivity and ultra-energy storage applications.

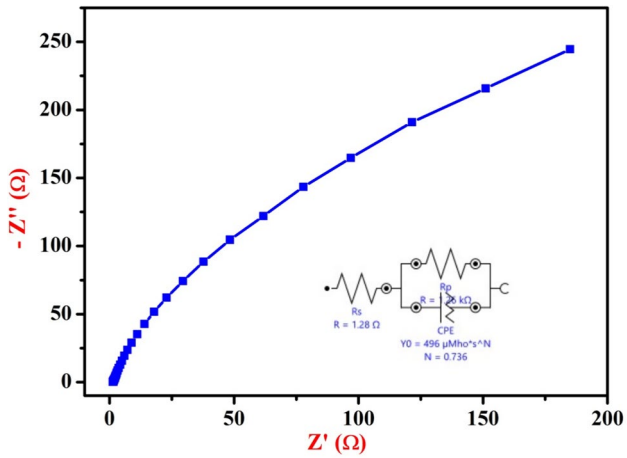

Fig. 11 Nyquest plot of ZMO-600 electrode material

4 Conclusion

$ZnMn_2O_4$ nanoparticls were successfully synthesized using the citric acid-mediated auto-combustion method. The X-ray diffraction indicates the existence of a tetragonal phase within the I41/amd space group. Morphological studies by FESEM indicated an agglomerated shape. Analysis through Fourier transform infrared spectroscopy revealed the presence of metal oxides in the tetrahedral (Mn–O) and octahedral (Zn–O) sites. The chemical compositions and oxidation states of Zn and Mn were studied using XPS. The BET analysis determined a specific surface area of 284.14 $m^2\ g^{-1}$ indicating a mesoporous nature, ideal for supercapacitor electrode applications. The dielectric loss (tanδ) suggests the material's suitablity for microwave applications, while the AC conductivity (σ_{ac}) increases with increasing frequencies. Evaluation of electrochemical performance revealed an enhanced specific capacitance value of 417.5 F g^{-1} for the current density of 1 A g^{-1} using a low-concentration of electrolyte (1 M KOH) with pseudocapacitance behaviour. Even after 5000 cycles, the materials exhibited an impressive Coulombic efficiency of 87%. The $ZnMn_2O_4$ electrode material demonstrated an energy

Table 2 Comparisons of specific capacitance and colulombic efficiency with a lower concentration in KOH

S No	Electrode material	Specific capacitance (Cs) F g-^{1}	Electrolyte	Method	Cycle stability	Ref
1	$ZnMn_2O_4$	122 F g^{-1} @ 0.3 A g^{-1}	6 M KOH	Combustion	84.8% even after 5000 cycles	[51]
2	$ZnMn_2O_4$	411 F g^{-1} @ 1 A g^{-1}	6 M KOH	Combustion	83% even after 4000 cycles	[50]
3	$ZnMn_2O_4$	158 F g^{-1}@2 mVs^{-1}	2 M KOH	Hydrothermal	1100	[31]
4	$ZnMn_2O_4$	380 F g^{-1} @ 0.5 A g^{-1}	2 M KOH	Hydrothermal	92% even after 2000 cycles	[15]
5	$ZnMn_2O_4$	776 F g^{-1} @ 5 mVs^{-1}	2 M KOH	Hydrothermal	91.7% even after 5000 cycles	[22]
6	$ZnMn_2O_4$	447 F g^{-1} @ 1 A g^{-1}	1 M KOH	Precipitation	-	[41]
7	$ZnMn_2O_4$	417.5 F g^{-1} @ 1 A g^{-1}	1 M KOH	Sol gel Auto-Combustion	87% even after 5000 cycles	Present study

density value of 5.83 $Whkg^{-1}$ and a power density value of 1000 Whg^{-1} at the current density value of 5 A g^{-1}. These findings suggest that the synthesized $ZnMn_2O_4$ nanoparticles are well-suited for electrical and electronic applications, especially energy storage devices.

Acknowledgements The authors would like to thank The Head, Department of Physics, Annamalai University for providing the analytical instrument purchased from DST-FIST-II.

Authors contribution **P. Deva**: Conceptualization, Data curation, Investigation Methodology, Writing-original draft. **S. Ravi:** Supervisor, Conceptualization, methodology, Formal analysis, and **C. Manoharan:** Data curation, visualization, Reviewing and Editing.

Funding The authors received no specific funding for this work.

Data Availability Data will be made available on request.

References

1. L. Li, Wu. Zhong, S. Yuan, X.-B. Zhang, Advances and challenges for flexible energy storage and conversion devices and systems. Energy Environ. Sci. **7**(7), 2101–2122 (2014). https://doi.org/10.1039/C4EE00318G
2. Gür, Turgut M. Review of electrical energy storage technologies, materials and systems: challenges and prospects for large-scale grid storage. Energy Environ Sci **11**(10), 2696–2767 (2018). https://doi.org/10.1039/C8EE01419A
3. Zhao, Xin, Hui Tian, Mingyao Zhu, Kai Tian, J. J. Wang, Feiyu Kang, and R. A. Outlaw. Carbon nanosheets as the electrode material in supercapacitors J. Power Sources **194**(2): 1208–1212 (2009). https://doi.org/10.1016/j.jpowsour.2009.06.004
4. Iro, Zaharaddeen S., C. Subramani, and S. S. Dash. A brief review on electrode materials for supercapacitor. Int. J. Electrochem. Sci. **11**(12), 10628–10643 (2016). https://doi.org/10.20964/2016.12.50
5. S. Xi, Y. Kang, Qu. Shengxiang, S. Han, Flexible supercapacitors on chips with interdigital carbon nanotube fiber electrodes. Mater Letter. **175**, 126–130 (2016). https://doi.org/10.1016/j.matlet.2016.03.143
6. Y.Q. Zhang, L. Li, S.J. Shi, Q.Q. Xiong, X.Y. Zhao, X.L. Wang, C.D. Gu, J.P. Tu, Synthesis of porous Co_3O_4 nanoflake array and its temperature behavior as pseudo-capacitor electrode. J. Power. Sources **256**, 200–205 (2014). https://doi.org/10.1016/j.jpowsour.2014.01.073
7. T. Huang, C. Zhao, R. Zheng, Y. Zhang, Hu. Zhibiao, Facilely synthesized porous $ZnCo_2O_4$ rodlike nanostructure for high-rate supercapacitors. Ionics **21**, 3109–3115 (2015). https://doi.org/10.1007/s11581-015-1491-2
8. Tiruye, Girum Ayalneh, David Muñoz-Torrero, Jesus Palma, Marc Anderson, and Rebeca Marcilla. Performance of solid state supercapacitors based on polymer electrolytes containing different ionic liquids. J. Power Sources 326, 560–568 (2016). https://doi.org/10.1016/j.jpowsour.2016.03.044
9. H. Wang, Fu. Qiang, C. Pan, "Green mass synthesis of graphene oxide and its MnO_2 composite for high performance supercapacitor. Electrochim. Acta **312**, 11–21 (2019). https://doi.org/10.1016/j.electacta.2019.04.178
10. Radhamani, A. V., M. Krishna Surendra, and MS Ramachandra Rao. "Tailoring the supercapacitance of Mn_2O_3 nanofibers by nanocompositing with spinel-$ZnMn_2O_4$.Materials&Design **139**, 162–171 (2018). https://doi.org/10.1016/j.matdes.2017.11.005
11. Ameri, Bahareh, Saied Saeed Hosseiny Davarani, Hamid Reza Moazami, and Hamideh Darjazi. Cathodic electrosynthesis of $ZnMn_2O_4/Mn_3O_4$ composite nanostructures for high performance supercapacitor applications. J. Alloys Compd. **720**, 408–416 (2017). https://doi.org/10.1016/j.jallcom.2017.05.271
12. Vigneshwaran, P., M. Kandiban, N. Senthil Kumar, V. Venkatachalam, R. Jayavel, and I. Vetha Potheher. A study on the synthesis and characterization of $CoMn_2O_4$ electrode material for supercapacitor applications. J.Mater. Sci: Mater Electron **27**, 4653–4658 (2016). https://doi.org/10.1007/s10854-016-4343-6
13. X. Zhai, W. Yang, M. Li, G. Lv, J. Liu, X. Zhang, Noncovalent hybrid of $CoMn_2O_4$ spinel nanocrystals and poly (diallyldimethylammonium chloride) functionalized carbon nanotubes as efficient electrocatalysts for oxygen reduction reaction. Carbon **65**, 277–286 (2013). https://doi.org/10.1016/j.carbon.2013.08.026
14. Guillén-López, Erwin Said, Florentino López-Urías, Emilio Muñoz-Sandoval, Maykel Courel-Piedrahita, Marciano Sanchez-Tizapa, Héctor Guillén-Bonilla, Verónica María Rodríguez-Betancourtt, Oscar Blanco-Alonso, Alex Guillén-Bonilla, and Juan Pablo Morán-Lázaro. High performance isopropanol sensor based on spinel $ZnMn_2O_4$ nanoparticles. Mater. Today Commun. **26**, 102138 (2021). https://doi.org/10.1016/j.mtcomm.2021.102138
15. V. Sannasi, K. Subbian, A facile synthesis of $ZnMn_2O_4/Mn_2O_3$ composite nanostructures for supercapacitor applications. Ceram. Int. **47**(9), 12300–12309 (2021). https://doi.org/10.1016/j.ceramint.2021.01.081
16. Y. Guan, Y. Feng, Mu. Yanping, L. Fang, H. Zhang, Yu. Wang, Ultra-tiny $ZnMn_2O_4$ nanoparticles encapsulated in sandwich-like carbon nanosheets for high-performance supercapacitors. Nanotechnol **27**(47), 475402 (2016). https://doi.org/10.1088/0957-4484/27/47/475402
17. Menaka, Mohammed Qamar, Samuel E. Lofland, Kandalam V. Ramanujachary, and Ashok K. Ganguli. Magnetic and photocatalytic properties of nanocrystalline $ZnMn_2O_4$.Bull.Mater. Sci. **32**: 231–237 (2009). https://doi.org/10.1007/s12034-009-0035-7
18. J. Li, S. Xiong, X. Li, Y. Qian, A facile route to synthesize multiporous $MnCo_2O_4$ and $CoMn_2O_4$ spinel quasi-hollow spheres with improved lithium storage properties. Nanoscale **5**(5), 2045–2054 (2013). https://doi.org/10.1039/C2NR33576J
19. C. Feng, W. Wang, X. Chen, S. Wang, Z. Guo, Synthesis and electrochemical properties of $ZnMn_2O_4$ anode for lithium-ion batteries. Electrochim. Acta **178**, 847–855 (2015). https://doi.org/10.1016/j.electacta.2015.08.070
20. H. Nan, W. Ma, Gu. Zhengxiang, B. Geng, X. Zhang, Hierarchical $NiMn_2O_4$@CNT nanocomposites for high-performance asymmetric supercapacitors. RSC Adv. **5**(31), 24607–24614 (2015). https://doi.org/10.1039/C5RA00979K
21. C. Zhang, A. Xie, W. Zhang, J. Chang, C. Liu, Gu. Linyang, X. Duo, F. Pan, S. Luo, $CuMn_2O_4$ spinel anchored on graphene nanosheets as a novel electrode material for supercapacitor. J. Energy Storage. **34**, 102181 (2021). https://doi.org/10.1016/j.est.2020.102181
22. Mani, M. Puratchi, V. Venkatachalam, K. Thamizharasan, and M. Jothibas. "Evaluation of cubic-like advanced $ZnMn_2O_4$ electrode for high-performance supercapacitor applications." J. Electron. Mater. **50**(8), 4381–4387 (2021). https://doi.org/10.1007/s11664-021-08962-0
23. N. Wang, X. Ma, Xu. Huayun, L. Chen, J. Yue, F. Niu, J. Yang, Y. Qian, Porous $ZnMn_2O_4$ microspheres as a promising anode

material for advanced lithium-ion batteries. Nano Energy **6**, 193–199 (2014). https://doi.org/10.1016/j.nanoen.2014.04.001
24. Toh, Rou Jun, Alex Yong Sheng Eng, Zdenek Sofer, David Sedmidubsky, and Martin Pumera. Ternary transition metal oxide nanoparticles with spinel structure for the oxygen reduction reaction." Chem.Electro.Chem. **2**(7), 982–987 (2015). https://doi.org/10.1002/celc.201500070
25. F.M. Courtel, Y. Abu-Lebdeh, I.J. Davidson, $ZnMn_2O_4$ nanoparticles synthesized by a hydrothermal method as an anode material for Li-ion batteries. Electrochim. acta **71**, 123–127 (2012). https://doi.org/10.1016/j.electacta.2012.03.108
26. L. Luo, H. Qiao, Ke. Chen, Y. Fei, Q. Wei, Fabrication of electrospun $ZnMn_2O_4$ nanofibers as anode material for lithium-ion batteries. Electrochim. Acta **177**, 283–289 (2015). https://doi.org/10.1016/j.electacta.2015.01.100
27. Cady, Clyde W., Graeme Gardner, Zachary O. Maron, Maria Retuerto, Yong Bok Go, Shreeda Segan, Martha Greenblatt, and G. Charles Dismukes. Tuning the electrocatalytic water oxidation properties of AB_2O_4 spinel nanocrystals A (Li, Mg, Zn) and B (Mn, Co) site variants of $LiMn_2O_4$. ACS Catalysis **5**(6), 3403–3410 (2015). https://doi.org/10.1021/acscatal.5b00265
28. M. Abdollahifar, S.-S. Huang, Y.-H. Lin, Y.-C. Lin, B.-Y. Shih, H.-S. Sheu, Y.-F. Liao, Wu. Nae-Lih, High-performance carbon-coated $ZnMn_2O_4$ nanocrystallite supercapacitors with tailored microstructures enabled by a novel solution combustion method. J. Power. Sources **378**, 90–97 (2018). https://doi.org/10.1016/j.jpowsour.2017.12.022
29. A. Varma, A.S. Mukasyan, A.S. Rogachev, K.V. Manukyan, Solution combustion synthesis of nanoscale materials. Chem. Rev. **116**(23), 14493–14586 (2016). https://doi.org/10.1021/acs.chemrev.6b00279
30. S. Sathyamoorthi, W. Tejangkura, M. Sawangphruk, Turning carbon-$ZnMn_2O_4$ powder in primary battery waste to be an effective active material for long cycling life supercapacitors: In situ gas analysis. Waste Manage. **109**, 202–211 (2020). https://doi.org/10.1016/j.wasman.2020.05.007
31. N. Guo, X.Q. Wei, X.L. Deng, X.J. Xu, Synthesis and property of spinel porous $ZnMn_2O_4$ microspheres. Appl. Surf. Sci. **356**, 1127–1134 (2015). https://doi.org/10.1016/j.apsusc.2015.08.185
32. Bhagwan, Jai, Nagesh Kumar, K. L. Yadav, and Yogesh Sharma. Probing the electrical properties and energy storage performance of electrospun $ZnMn_2O_4$ nanofibers. Solid State Ion. **321**, 75–82 (2018). https://doi.org/10.1016/j.ssi.2018.04.007
33. S. Yang, M. Zhang, Wu. Xianwen, Wu. Xiangsi, F. Zeng, Y. Li, S. Duan, D. Fan, Y. Yang, Wu. Xianming, The excellent electrochemical performances of $ZnMn_2O_4/Mn_2O_3$: the composite cathode material for potential aqueous zinc ion batteries. J. Electro. Chem. **832**, 69–74 (2019). https://doi.org/10.1016/j.jelechem.2018.10.051
34. Dhinesh, S., Bommireddy Purusottam Reddy, M. Priyadharshini, T. Pazhanivel, S. Seenivasan, Si-Hyun Park, Mohd Shkir, and F. Maiz,Thermal nanoarchitectonics with $NiMn_2O_4$ binary nanocomposite as a superior electrode material for the fabrication of high performance supercapacitors. Inorg. Chem. Commun, **143**, 109793 (2022). https://doi.org/10.1016/j.inoche.2022.109793.
35. M.R. Kim, Reddi Mohan NaiduKalla, Seok Kim, Mi-Ra Kim, and Il Kim $NiMn_2O_4$ nanosheet-decorated hierarchically porous polyaromatic carbon spheres for high-performance supercapacitors. Chem. Electro. Chem. **4**(5), 1214–1221 (2017). https://doi.org/10.1002/celc.201700023
36. J. Bhagwan, BN Vamsi Krishna, and Jae Su Yu, Template and sol-gel routed $CoMn_2O_4$ nanofibers for supercapacitor applications. Int. J. Energy Res. **45**(13), 19413–19422 (2021). https://doi.org/10.1002/er.7096
37. Yeow, S. C., W. L. Ong, A. S. W. Wong, and G. W. Ho.Template-free synthesis and gas sensing properties of well-controlled porous tin oxide nanospheres. Sens. ActuatorsB: Chem. **143**, 295–301 (2009).https://doi.org/10.1016/j.snb.2009.08.050
38. J. Zhao, F. Wang, Su. Panpan, M. Li, J. Chen, Q. Yang, C. Li, Spinel $ZnMn_2O_4$ nanoplate assemblies fabricated via escape-by-crafty-scheme strategy. J. Mater. Chem. **22**(26), 13328–13333 (2012). https://doi.org/10.1039/C2JM32261G
39. Menaka, Mohammed Qamar, Samuel E. Lofland, Kandalam V. Ramanujachary, and Ashok K. Ganguli. "Magnetic and photocatalytic properties of nanocrystalline $ZnMn_2O_4$." Bull Mater Sci **32**, 231–237 (2009). https://doi.org/10.1007/s12034-009-0035-7
40. Rahman, Mohammed M., George Gruner, Mohammed Saad Al-Ghamdi, Muhammed A. Daous, Sher Bahadar Khan, and Abdullah M. Asiri. Chemo-sensors development based on low-dimensional codoped Mn_2O_3-ZnO nanoparticles using flat-silver electrodes. Chem. Cent. J .**7**, 1–12 (2013). https://doi.org/10.1186/1752-153X-7-60
41. Fang, Qun, Chuansheng Chen, Zhi Yang, Xi'an Chen, Xiaohua Chen, and Tiangui Liu. Synthetization and electrochemical performance of pomegranate-like $ZnMn_2O_4$ porous microspheres. J. Alloys and Comp. **826**, 154084 (2020). https://doi.org/10.1016/j.jallcom.2020.154084
42. Stranick, Michael A. Mn2O3 by XPS. Surf Sci Spectra **6**(1), 39–46 (1999). https://doi.org/10.1116/1.1247889
43. Aruchamy, Kanakaraj, Radha Nagaraj, Halanur M. Manohara, Maalige R. Nidhi, Dibyendu Mondal, Debasis Ghosh, and Sanna Kotrappanavar Nataraj. One-step green route synthesis of spinel $ZnMn_2O_4$ nanoparticles decorated on MWCNTs as a novel electrode material for supercapacitor. Mater. Sci. Eng: B **252**, 114481 (2020). https://doi.org/10.1016/j.mseb.2019.114481
44. Zhang, Ruitao, Jie Fang Li, and Dwight Viehland. Effect of Aliovalent Substituents on the Ferroelectric Properties of Modified Barium Titanate Ceramics-Relaxor Ferroelectric Behavior. J. Am. Ceram. Soc. **87**(5): 864–870 (2004). https://doi.org/10.1111/j.1551-2916.2004.00864.x
45. Radoń, Adrian, Dariusz Łukowiec, Marek Kremzer, Jarosław Mikuła, and Patryk Włodarczyk. Electrical conduction mechanism and dielectric properties of spherical shaped Fe3O4 nanoparticles synthesized by co-precipitation method. Materials **11**(5), 735 (2018). https://www.mdpi.com/1996-1944/11/5/735#
46. Sutton, Willard H. Microwave processing of ceramic materials. Am. Ceram. Soc. Bull. **68**(2), 376–386 (1989).
47. Kumari, Naveen, Vinod Kumar, and S. K. Singh. Structural, dielectric and magnetic investigations on Al^{3+} substituted Zn-ferrospinels. RSC Advances **5**(47), 37925–37934 (2015). https://doi.org/10.1039/C5RA03745J
48. Khan, Ziaul Raza, Mohd Shkir, V. Ganesh, I. S. Yahia, and S. AlFaify. A facile microwave-assisted synthesis of novel $ZnMn_2O_4$ nanoparticles and their structural, morphological, optical, surface area, and dielectric studies. Ind. J. Phy. **95**, 43–49 (2021). https://doi.org/10.1007/s12648-020-01695-6
49. Deva, P., S. Ravi, and E. Manikandan. Facile synthesis of CuMn2O4 nanoparticles for efficient of high performance electrode materials for supercapacitor application. Ceram.Int.**50**, 11916–11927 (2024). https://doi.org/10.1016/j.ceramint.2024.01.095
50. Hussain, Sk Khaja, and Jae Su Yu. Cobalt-doped zinc manganese oxide porous nanocubes with controlled morphology as positive electrode for hybrid supercapacitors. Chem.Eng. J. **361**, 1030–1042 (2019). https://doi.org/10.1016/j.cej.2018.12.152
51. T. Huang, C. Zhao, Z. Qiu, J. Luo, Hu. Zhibiao, Hierarchical porous $ZnMn_2O_4$ synthesized by the sucrose-assisted combustion method for high-rate supercapacitors. Ionics **23**, 139–146 (2017). https://doi.org/10.1007/s11581-016-1817-8

52. Deva, P., and S. Ravi. Enhanced electrochemical performance of $NiMn_2O_4$ nanomaterial synthesized using auto-combustion method. J. Sol-Gel Sci. Technol. 1–16 (2024). https://doi.org/10.1007/s10971-024-06349-1
53. Sim, Cheng-Kim, S. A. Razali, Siti Rohana Majid, and Noor Zalina Mahmood. Synthesis and Characterization of Ternary Mesoporous Carbon/$ZnMn_2O_4$ for Supercapacitor Application. J. Electron. Mater. **49**, 1024–1035 (2020). https://doi.org/10.1007/s11664-019-07733-2